

# Interfacial Regulation of Electron-enhanced Co<sub>2</sub>P–CuP<sub>2</sub> Sheet-like Heterostructure as a Robust Bifunctional Electrocatalyst for Overall Water Splitting and Zn–H<sub>2</sub>O Cell

Lixia Wang,<sup>[a]</sup> Yunru Zhao,<sup>[a]</sup> Zhiyang Huang,<sup>[a]</sup> Xianfa Rao,<sup>\*,[b]</sup> Man Guo,<sup>[a]</sup> Tayirjan Taylor Isimjan,<sup>\*,[c]</sup> and Xiulin Yang<sup>\*,[a]</sup>

Constructing the precious metal-free bifunctional electrocatalysts for hydrogen evolution reaction (HER) and oxygen evolution reaction (OER) is highly desirable for overall water splitting and energy conversion devices in an alkaline medium. Here, the interface regulation strategy aims to synthesize a sheet-like Co<sub>2</sub>P–CuP<sub>2</sub> heterostructure supported on nickel foam (NF) through hydrothermal reaction, electrodeposition and phosphating treatment. The Co<sub>2</sub>P–CuP<sub>2</sub>/NF exhibits extraordinary electrocatalytic performance with overpotentials of 220 mV and 93 mV for OER and HER at a current density of 10 mA cm<sup>-2</sup>, respectively. Remarkably, an electrolyzer cell originated from Co<sub>2</sub>P–CuP<sub>2</sub>/NF electrodes required an ultralow cell

voltage of 1.77 V@500 mA cm<sup>-2</sup> and 2.38 V@1000 mA cm<sup>-2</sup> for overall water splitting with prominent stability of at least 160 h. In addition, the Zn–H<sub>2</sub>O cell is assembled with Co<sub>2</sub>P–CuP<sub>2</sub>/NF as the cathode, achieving a high power density of 19.8 mW cm<sup>-2</sup> and long-term stability of 120 h. The electron transfer between Co and Cu species in the Co<sub>2</sub>P–CuP<sub>2</sub>/NF heterojunction can effectively improve the interaction between the active sites and the intermediates, thereby enhancing the electrocatalytic activity. This work opens up new insights into the preparation of highly active and durable bimetallic phosphide catalysts for water splitting and Zn–H<sub>2</sub>O cells.

## Introduction

The environmental problems and energy crisis caused by excessive use of fossil fuels have led to the demand for renewable energy technologies.<sup>[1]</sup> Electrochemical water splitting is a primary step towards sustainable clean energy to accelerate the HER (2H<sup>+</sup> + 2e<sup>-</sup> → H<sub>2</sub>) and OER (4OH<sup>-</sup> → O<sub>2</sub> + 2H<sub>2</sub>O) by applying electrocatalysts to produce hydrogen and oxygen.<sup>[2]</sup> Currently, although noble metal-based materials (such as Pt, RuO<sub>2</sub> and IrO<sub>2</sub>) are the most advanced catalysts,<sup>[3]</sup> the prohibitive expense and scarcity severely hinder their large-scale application.<sup>[4]</sup> Therefore, it is impending to exploit the catalysts with high-efficiency and affordable to reduce overpotential and improve water splitting efficiency.<sup>[5]</sup> To overcome these handicaps, significant research efforts have been devoted

to developing transition metal-based catalysts as alternatives for water splitting.<sup>[6]</sup>

Currently, transition metal phosphides (TMPs) have evoked substantial attention in the field of electrocatalysis for overall water splitting by their high electrical conductivity, earth-abundant, good durability, and high catalytic performance.<sup>[7]</sup> According to previous studies, TMPs are a pre-catalyst for OER in alkaline medium, which will form a layer of oxide or hydroxide on the catalyst surface as the active center.<sup>[8]</sup> The obtained active intermediate can adjust the binding energy in the OER process, thereby contributing to the improvement of the catalytic activity.<sup>[9]</sup> For HER, a single metal phosphide exhibits unsatisfactory catalytic activity due to the fact that the Gibbs free energy (ΔG<sub>H<sup>+</sup></sub>) of hydrogen adsorption is far from zero.<sup>[10]</sup> As compared with single metal phosphide, the negatively charged P atoms in the bimetallic phosphides not only serve as a basis for capturing positively charged protons but also provide high H<sub>2</sub> dissociation activity to increase HER activity.<sup>[11]</sup> Additionally, in various TMPs catalysts, cobalt-based phosphides are widely used for water splitting. Most of the previous reports have confirmed that the catalytic activity of cobalt phosphide can adjust the surface electronic structure by constructing heterostructure interfaces, controlling its morphology or combining it with a conductive substrate.<sup>[12]</sup> For instance, Hua and co-workers reported coupled CoP nanosheet array with Co<sub>2</sub>P nanoparticles exhibit small overpotentials of 68 and 256 mV to drive 10 mA cm<sup>-2</sup> for HER and OER, respectively.<sup>[13]</sup> A study from Jin et al. indicated that a hierarchical CoP@Ni<sub>2</sub>P grown on nickel foam with remarkable HER performance as an effective pH-universal catalyst.<sup>[14]</sup> Li et al proposed a Co<sub>2</sub>P–Fe<sub>2</sub>P/NF with an abundant and strongly electronic coupled interface,

[a] L. Wang, Y. Zhao, Z. Huang, M. Guo, Prof. X. Yang  
Guangxi Key Laboratory of Low Carbon Energy Materials  
School of Chemistry and Pharmaceutical Sciences  
Guangxi Normal University  
Guilin 541004 (P. R. China)  
E-mail: xlyang@gxnu.edu.cn

[b] Dr. X. Rao  
School of Resources and Environmental Engineering  
Jiangxi University of Science and Technology  
Ganzhou 341000 (P. R. China)  
E-mail: raoxianfa@126.com

[c] Dr. T. T. Isimjan  
Saudi Arabia Basic Industries Corporation (SABIC) at King Abdullah  
University of Science and Technology (KAUST)  
Thuwal 23955-6900 (Saudi Arabia)  
E-mail: isimjant@sabic.com

Supporting information for this article is available on the WWW under <https://doi.org/10.1002/cctc.202101933>

which not only ensures rapid charge transfer and improves reaction kinetics but also enables the charge redistributed between  $\text{Co}_x\text{P}$  and  $\text{Fe}_2\text{P}$ , thereby optimizing the adsorption capacity of the reactants for the overall water splitting.<sup>[15]</sup> Among the numerous TMPs, there are few reports on the application of  $\text{CuP}_2$  in the field of electrocatalytic overall water splitting.<sup>[16]</sup> Moreover, the electrocatalytic properties of  $\text{Co}_x\text{P}$  and  $\text{Cu}_2\text{P}$  hybrid materials have not yet been investigated.

Accordingly, we synthesized self-supported  $\text{Co}_2\text{P-CuP}_2$  with layered sheet-like on NF via a novel one-step low temperature hydrothermal, constant potential electrodeposition, and phosphating approach. The electrocatalyst demonstrates distinguished bifunctional catalytic activity and long-term stability for overall water splitting in alkaline electrolyte. Furthermore, the assembled cell of  $\text{Co}_2\text{P-CuP}_2/\text{NF}$  can drive the current densities of 500 and 1000  $\text{mA cm}^{-2}$  at low voltages of 1.77 and 2.38 V, respectively, which was superior to Pt/C-RuO<sub>2</sub> based electrolyzer. The extraordinary electrocatalytic performance of the  $\text{Co}_2\text{P-CuP}_2/\text{NF}$  heterostructure is ascribed to the sheet-like heterostructure providing a larger active surface area, but also the exceptionally interaction between  $\text{Co}_2\text{P}$  and  $\text{CuP}_2$  interface. In particular, the Zn-H<sub>2</sub>O cell assembled with  $\text{Co}_2\text{P-CuP}_2/\text{NF}$  as the cathode delivered a power density of 19.8  $\text{mW cm}^{-2}$  and displayed outstanding stability for 120 h. Consequently, this work is highly promising for overall water splitting and renewable energy conversion applications.

## Results and Discussion

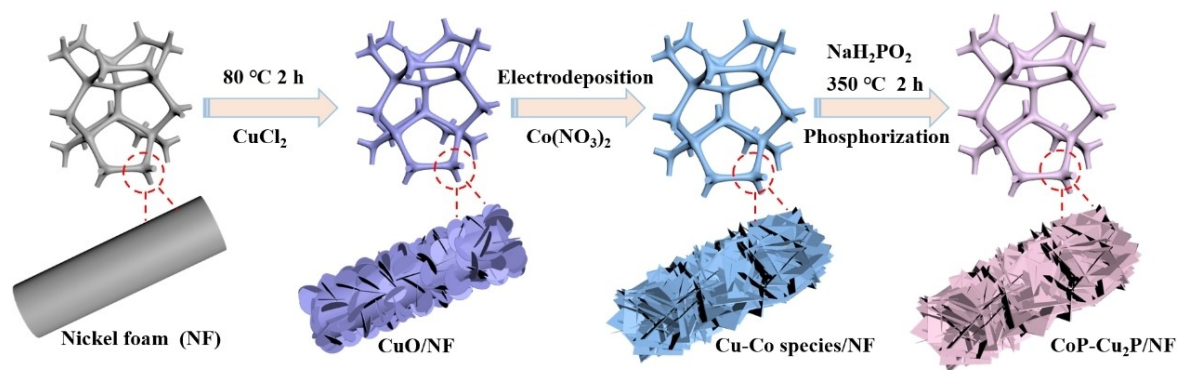
### Synthetic strategy analysis

The fabrication of  $\text{Co}_2\text{P-CuP}_2$  on the NF surface involves a three-step synthesis strategy, as illustrated in Scheme 1. Firstly,  $\text{CuCl}_2$  was dissolved in 15 mL of deionized water, and the pH was adjusted by adding excessive  $\text{NH}_3 \cdot \text{H}_2\text{O}$  (750  $\mu\text{L}$ ) to form a copper ammonium complex. Then, the NF was placed on an oblique angle and hydrothermally treated at 80 °C for 2 h to form  $\text{CuO/NF}$  (Figure S2). Subsequently, the Co-Cu precursor was obtained by electrodepositing Co species on the  $\text{CuO/NF}$  substrate. Finally, the Co-Cu precursor was converted to

$\text{Co}_2\text{P-CuP}_2/\text{NF}$  by phosphating with  $\text{NaH}_2\text{PO}_2$  as P source at 350 °C for 2 h under  $\text{N}_2$  atmosphere.

### Structural and morphological characterizations

The phase chemical composition of the catalysts was elucidated by X-ray diffraction (XRD). As shown in Figure S3a, the XRD pattern of the  $\text{CuO/NF}$  precursor, in which the diffraction peak is well defined as the peak of  $\text{CuO}$  (JCPDS: 01-1117).<sup>[17]</sup> Figure 1a shows the XRD patterns of  $\text{Co}_2\text{P-CuP}_2/\text{NF}$  where all XRD peaks can be attributed to the standard characteristic peaks. The peaks at 40.97°, 43.30°, 44.07°, 48.71°, 50.37°, 52.03° and 56.20° corresponding to the (201), (211), (130), (031), (310), (002) and (320) of  $\text{Co}_2\text{P}$  (JCPDS: 32-0306),<sup>[7b,18]</sup> at 30.9°, 44.8°, 50.4° and 55.0° can be indexed to the (111), (-213), (202) and (023) planes of  $\text{CuP}_2$  (JCPDS: 65-1274)<sup>[19]</sup>. The peaks at around 45°, 52.5° and 77.1° originating from the metallic nickel (JCPDS: 03-1051) derived from NF. The XRD patterns of the control samples affirmed that the corresponding XRD patterns well match that of  $\text{Co}_2\text{P}$  (JCPDS: 32-0306) and  $\text{CuP}_2$  (JCPDS: 65-1274) in Figures S3b and S3c. The surface morphology of the prepared catalysts was investigated by scanning electron microscopy (SEM) and transmission electron microscopy (TEM), respectively. SEM revealed that there were differences in morphology of the prepared  $\text{CuO/NF-x}$  ( $x=0.2, 0.4, 0.6, 0.8, 1.0$ ) prepared with different Cu contents. The obtained  $\text{CuO/NF}$  grew from small flakes to large flakes and gradually became dense as the amount of Cu species increased from 0.2 mmol to 1.0 mmol until a plurality of sheet-like agglomerated together at 1.0 mmol (Figure S4). As illustrated in Figure 1b, the catalyst surface was transformed into layered nanoplatelets after Co species were deposited on the  $\text{CuO/NF-0.6}$  surface and phosphating treatment ( $\text{Co}_2\text{P-CuP}_2/\text{NF}$ ). Layered sheet-like morphology was further confirmed by transmission electron morphology (TEM) image of  $\text{Co}_2\text{P-CuP}_2/\text{NF}$  (Figure 1c). The lattice fringes of  $\text{Co}_2\text{P-CuP}_2/\text{NF}$  were observed from high-resolution TEM (HR-TEM) images. The well-resolved lattice fringes with 0.239 nm, 0.227 and 0.224 nm are associated with the (211) (201) and (121) crystal planes of  $\text{Co}_2\text{P}$ , whereas the lattice fringes with inter-planar spacing of 0.173 nm corre-



**Scheme 1.** Schematic illustration of the fabrication of  $\text{Co}_2\text{P-CuP}_2/\text{NF}$  electrocatalysts.

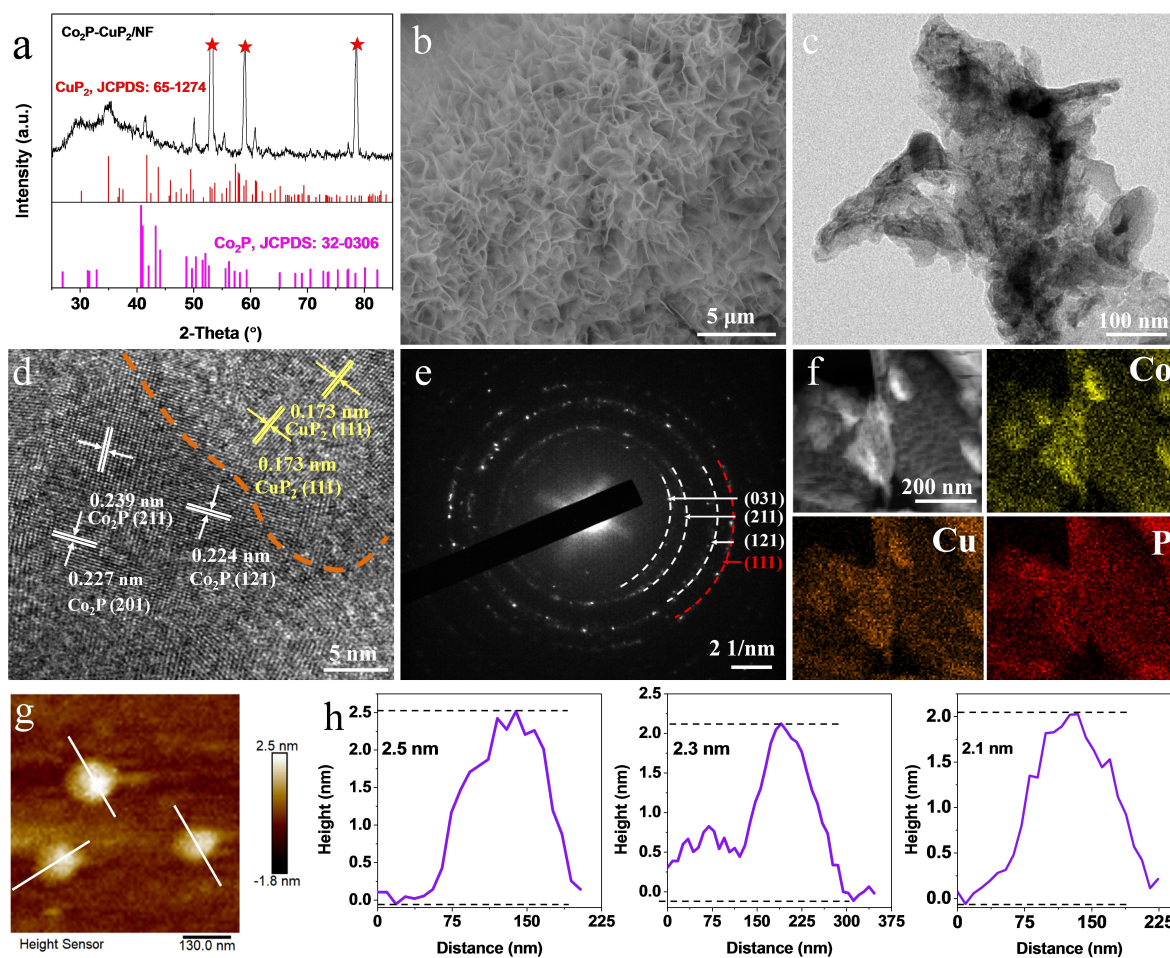


**Figure 1.** (a) XRD pattern, (b) SEM image, (c) TEM image, (d) high-resolution TEM image and (e) SAED image of  $\text{Co}_2\text{P-CuP}_2/\text{NF}$ . (f) HAADF-STEM image and corresponding element mappings, and (g-h) AFM image and the corresponding height profile of  $\text{Co}_2\text{P-CuP}_2/\text{NF}$ .

sponds to the (111) crystal plane of  $\text{CuP}_2$  (Figure 1d). Moreover, the selective area electron diffraction (SAED) pattern (Figure 1e) confirmed that the diffraction ring can be indexed to the (111) plane of  $\text{CuP}_2$  and the (211), (201) and (121) planes of  $\text{Co}_2\text{P}$ , respectively, which is consistent with the XRD analysis results. In addition, the high-angle circular dark-field scanning TEM (HAADF-STEM) image and corresponding elemental mappings reveal that Co, Cu and P elements are uniformly distributed on  $\text{Co}_2\text{P-CuP}_2/\text{NF}$  (Figure 1f). Energy dispersive X-ray (EDX) pattern (Figure S5) shows obvious signals of Co, Cu, and P in  $\text{Co}_2\text{P-CuP}_2/\text{NF}$ . Atomic force microscopy (AFM) verified the morphology of  $\text{Co}_2\text{P-CuP}_2/\text{NF}$  sheet-like with a thickness of approximately 2.3 nm (Figures 1g and 1h). Furthermore, the ICP-MS results showed the true content of metal elements, in which the fractions of Co and Cu were 5.41 wt% and 10.56 wt%, respectively, and the Co/Cu molar ratio was 1/1.81 (Table S1).

### XPS analysis

X-ray photoelectron spectroscopy (XPS) was performed to further detect the elemental composition and the chemical

states of the as-obtained samples. As depicted in Figure S6a, the full survey spectrum of  $\text{Co}_2\text{P-CuP}_2/\text{NF}$  demonstrates the existence of Co, Cu and P elements, which is consistent with the XRD and TEM results. The high-resolution C 1s spectrum was deconvoluted into four peaks, including C=O (284.0 eV), C-C (284.8 eV) and C-O (286.0 eV). Meanwhile, the binding energies based on C 1s as the standard for correction (Figure S6b). As displayed in Figure 2a, the high-resolution XPS spectra of Co 2p in  $\text{Co}_2\text{P-CuP}_2/\text{NF}$  showed Co 2p<sub>3/2</sub> peaks at 778.10 eV, 781.04 eV, and 785.13 eV are deconvoluted into Co-P, Co-O and satellite peak.<sup>[20]</sup> For elemental Cu, the Cu 2p spectrum alone is not sufficient to distinguish Cu<sup>+</sup> from Cu<sup>0</sup> due to the peak positions.<sup>[21]</sup> The Cu LMM spectrum is used to determine the Cu valence state because the kinetic energy of the Cu<sup>0</sup> spiral peak is about 3 eV higher than the Cu<sup>+</sup> spiral peak.<sup>[22]</sup> The Auger electron spectrum of Cu LMM was also obtained in Figure S7. The  $\text{Co}_2\text{P-CuP}_2/\text{NF}$  showing a Cu LMM spectrum similar to  $\text{CuP}_2/\text{NF}$  with a peak position at 570.0 eV can be attributed to Cu<sup>+</sup>.<sup>[22b]</sup> Wherefore, the peak located at 931.95 eV in the Cu 2p<sub>3/2</sub> spectrum of  $\text{Co}_2\text{P-CuP}_2/\text{NF}$  is assigned to Cu<sup>+</sup>, while the binding energy at 933.97 eV is attributed to Cu<sup>2+</sup>, as well as two satellite peaks at 939.52 eV and 943.57 eV

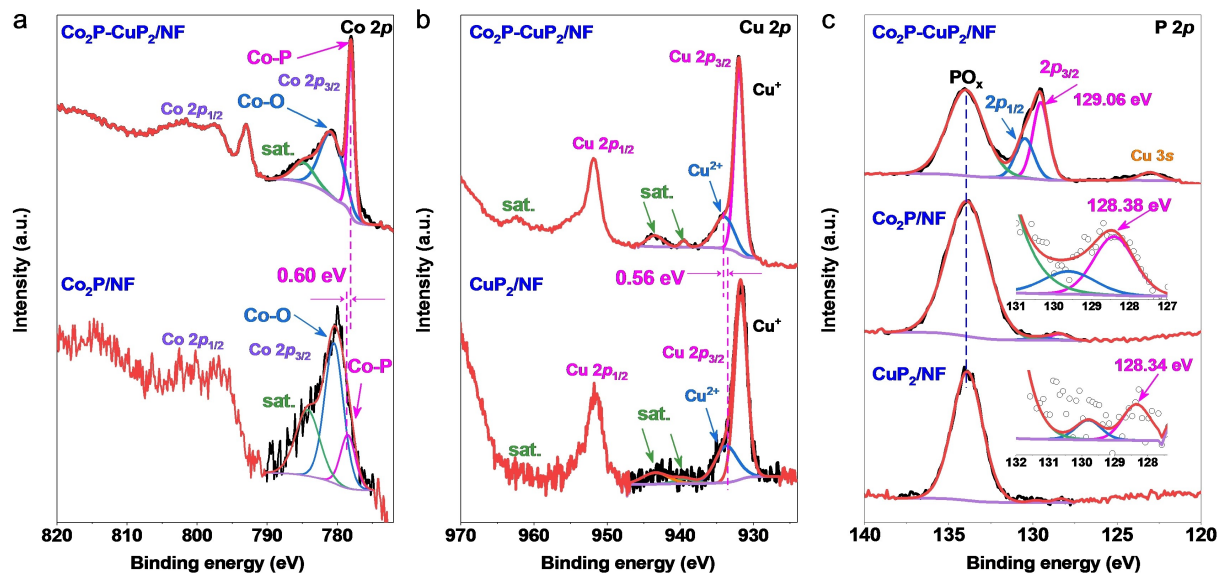


Figure 2. (a) High-resolution XPS spectra of (a) Co 2p of  $\text{Co}_2\text{P-CuP}_2/\text{NF}$  and  $\text{Co}_2\text{P/NF}$ , (b) Cu 2p of  $\text{Co}_2\text{P-CuP}_2/\text{NF}$  and  $\text{CuP}_2/\text{NF}$ , and (c) P 2p of all samples.

(Figure 2b).<sup>[23]</sup> The P 2p XPS spectra showed two fitted peaks at 129.06 and 130.08 eV can be assigned to the  $2p_{3/2}$  and  $2p_{1/2}$  of  $\text{Co}_2\text{P-CuP}_2/\text{NF}$ , respectively (Figure 2c).<sup>[24]</sup> For the peak of P–O, which derived from the oxidation of the surface sample exposed to air.<sup>[25]</sup> Interestingly, the Co  $2p_{3/2}$  peak of  $\text{Co}_2\text{P-CuP}_2/\text{NF}$  showed a negative shift approximately of 0.60 eV compared to  $\text{Co}_2\text{P/NF}$ .<sup>[26]</sup> In contrast, the  $\text{Cu}^{2+}$  binding energy of  $\text{Co}_2\text{P-CuP}_2/\text{NF}$  had a positive shift of 0.56 eV compared to that of  $\text{CuP}_2/\text{NF}$ . The above results demonstrated that electronic reconstruction occurs between different components facilitating electron transfer from  $\text{Co}_2\text{P}$  to  $\text{CuP}_2$ ,<sup>[15]</sup> confirming the existence of strong electron interaction between the two substances. This strong electron interaction can effectively regulate the binding energy of the active sites and intermediates, thus improving the electrocatalytic performance.<sup>[7a,27]</sup>

### Electrocatalytic performance

To evaluate the OER performance of the synthesized samples in 1 M KOH solution. First, the polarization curves of  $\text{CuO/NF-x}$  (Figure S8) proved that  $\text{CuO/NF-0.6}$  exhibits the best catalytic activity and was used for subsequent electrodeposition. Additionally, the optimized electrodeposition time was 5 min both toward OER and HER (Figure S9). As expected, the  $\text{Co}_2\text{P-CuP}_2/\text{NF}$  possessed a splendid OER performance with an overpotential of 220 mV at  $10 \text{ mA cm}^{-2}$ , which is comparable to  $\text{RuO}_2/\text{NF}$  ( $\eta_{10}=214 \text{ mV}$ ) but substantially lower than the  $\text{Co}_2\text{P/NF}$  ( $\eta_{10}=262 \text{ mV}$ ),  $\text{CuP}_2/\text{NF}$  ( $\eta_{10}=361 \text{ mV}$ ),  $\text{NF-P}$  and  $\text{NF}$  (Figure 3a). However, the comparison of  $\eta_{10}$  is not sufficient to confirm the superiority of the  $\text{Co}_2\text{P-CuP}_2/\text{NF}$ . Therefore, the overpotentials with current densities of 50 and  $100 \text{ mA cm}^{-2}$  was selected as the comparison parameters. The corresponding results are displayed in Figure 3b. The  $\eta_{50}$  and  $\eta_{100}$  of  $\text{Co}_2\text{P-CuP}_2/\text{NF}$  are very small, manifesting that it has the

optimal OER performance. Tafel slope is another pivotal parameter for the evaluation of the electrocatalytic activity and its trend is as follows:  $\text{Co}_2\text{P-CuP}_2/\text{NF}$  ( $68 \text{ mV dec}^{-1}$ ) <  $\text{Co}_2\text{P/NF}$  ( $73 \text{ mV dec}^{-1}$ ) <  $\text{RuO}_2/\text{NF}$  ( $97 \text{ mV dec}^{-1}$ ) <  $\text{CuP}_2/\text{NF}$  ( $128 \text{ mV dec}^{-1}$ ) in Figure 3c.  $\text{Co}_2\text{P-CuP}_2/\text{NF}$  has a smaller Tafel slope value, implying faster reaction kinetics.<sup>[28]</sup> Impressively, the excellent performance of  $\text{Co}_2\text{P-CuP}_2/\text{NF}$  is also superior to the most recently reported OER catalysts (Figure 3d and Table S2). Meanwhile, electrochemical impedance spectroscopy (EIS) can be performed to characterize the charge transfer resistance of electrocatalysis.<sup>[29]</sup> The charge-transfer resistance ( $R_{ct}$ ) of  $\text{Co}_2\text{P-CuP}_2/\text{NF}$  is much smaller than  $\text{Co}_2\text{P/NF}$ ,  $\text{CuP}_2/\text{NF}$  and  $\text{RuO}_2/\text{NF}$ , verifying a faster charge transfer process between electrolyte and electrode (Figure 3e).<sup>[30]</sup> In addition, the double-layer capacitance ( $C_{dl}$ ) derived from the cyclic voltammetry (CV) curve in the non-Faradaic range (Figure S10–12). The  $C_{dl}$  value of  $\text{Co}_2\text{P-CuP}_2/\text{NF}$  is  $45 \text{ mF cm}^{-2}$ , which is 2.1-, 3.0-, and 5.6-fold higher than  $\text{Co}_2\text{P/NF}$  ( $21 \text{ mF cm}^{-2}$ ),  $\text{RuO}_2/\text{NF}$  ( $15 \text{ mF cm}^{-2}$ ) and  $\text{CuP}_2/\text{NF}$  ( $8 \text{ mF cm}^{-2}$ ), respectively (Figure 3f). And the electrochemically active surface area (ECSA) is calculated based on  $C_{dl}$  (Supporting Information). The resultant  $\text{Co}_2\text{P-CuP}_2/\text{NF}$  manifests the largest ECSA value of  $750 \text{ cm}^{-2}$  (normalized to per  $\text{cm}^2$  of electrode area), indicating that it has more abundant active to promote electrocatalytic activity (Figure 3g).<sup>[31]</sup> As shown in Figure 3h, the multi-step chronoamperometry curve reflects that  $\text{Co}_2\text{P-CuP}_2/\text{NF}$  can respond rapidly to different current densities and reach a stable state, implying  $\text{Co}_2\text{P-CuP}_2/\text{NF}$  has extraordinary stability. Besides, the long-term stability test of  $\text{Co}_2\text{P-CuP}_2/\text{NF}$  was carried out using the constant current method. Figure 3i illustrated that the  $\text{Co}_2\text{P-CuP}_2/\text{NF}$  heterostructure can maintain stability at current densities of  $100 \text{ mA cm}^{-2}$  and  $10 \text{ mA cm}^{-2}$  for 100 and 200 h, respectively, and no noticeable potential augment was observed.

The HER activities of the as-prepared samples were also evaluated in 1.0 M KOH. The  $\text{Co}_2\text{P-CuP}_2/\text{NF}$  demonstrated

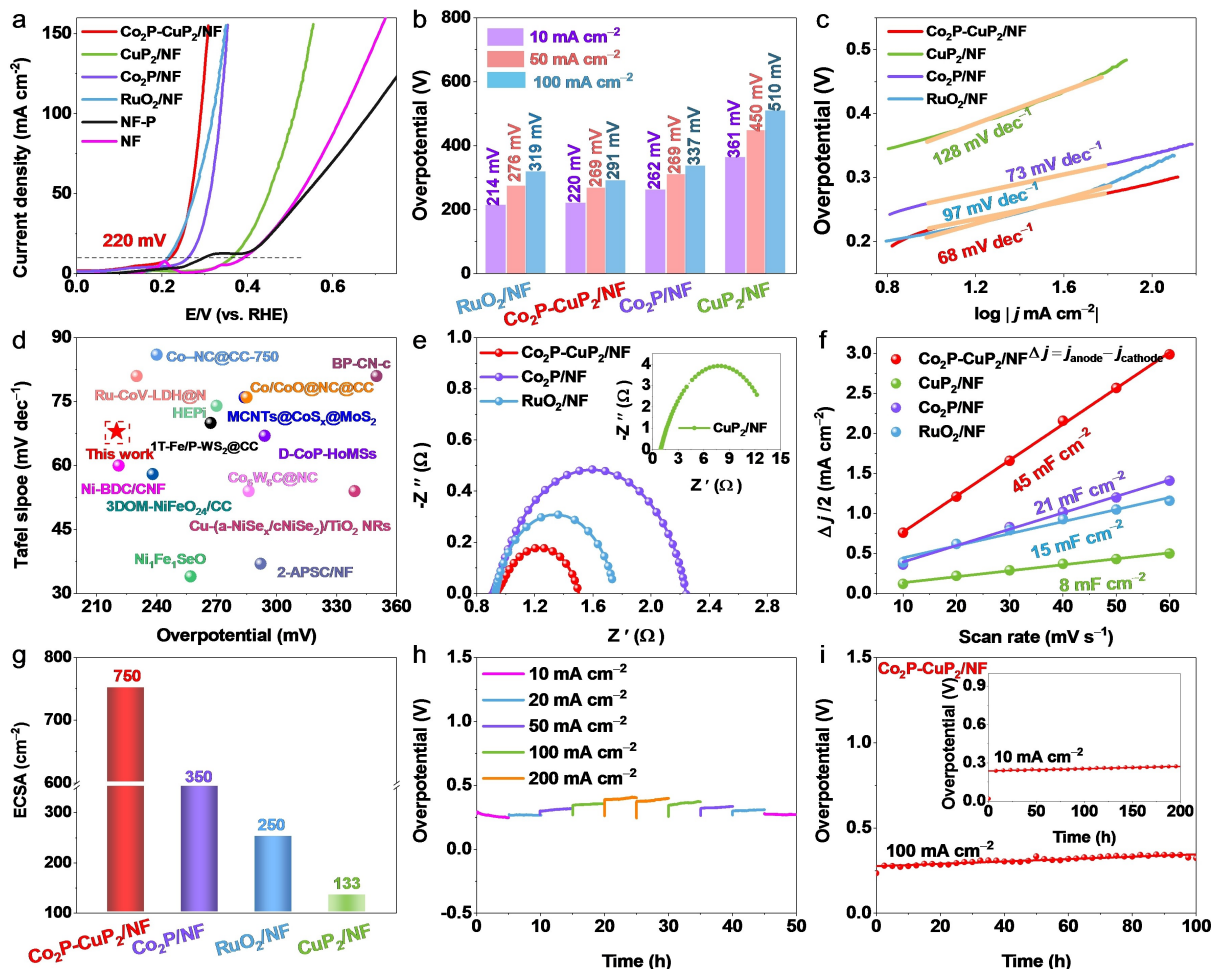


**Figure 3.** OER performance of prepared catalysts in 1.0 M KOH. (a) LSV polarization curves, (b) Overpotential comparison at 10, 50, and 100 mA cm<sup>-2</sup>, (c) corresponding Tafel slopes, (d) comparison with the overpotentials of recently reported catalysts for OER activity at 10 mA cm<sup>-2</sup>, (e) electrochemical impedance spectroscopy (EIS), (f) double layer capacitance ( $C_{dl}$ ), and (g) comparison the electrochemical active surface area (ECSA). (h) Multi-step chronopotentiometric curve at different current densities from 10 to 200 mA cm<sup>-2</sup> for Co<sub>2</sub>P–CuP<sub>2</sub>/NF, and (i) stability tests of Co<sub>2</sub>P–CuP<sub>2</sub>/NF electrodes.

outstanding catalytic activity with an overpotential of 93 mV at the current density of 10 mA cm<sup>-2</sup>, which is superior to Co<sub>2</sub>P/NF (135 mV), CuP<sub>2</sub>/NF (214 mV), NF–P and NF in Figure 4a. Meanwhile, the overpotentials of Co<sub>2</sub>P–CuP<sub>2</sub>/NF were 93, 139, and 166 mV at current densities of 10, 50, and 100 mA cm<sup>-2</sup>, respectively (Figure 4b). It is much lower than other contrast samples apart from Pt/C/NF. Notably, the performance of Co<sub>2</sub>P–CuP<sub>2</sub>/NF is close to Pt–C/NF at high current density (> 122 mA cm<sup>-2</sup>). To further understand the HER kinetic mechanism, Tafel slope analysis is revealed in Figure 4c. The Tafel slope of Co<sub>2</sub>P–CuP<sub>2</sub>/NF is 61 mV dec<sup>-1</sup>, which is much lower than the Co<sub>2</sub>P/NF (63 mV dec<sup>-1</sup>) and the CuP<sub>2</sub>/NF (134 mV dec<sup>-1</sup>), indicating the HER process follows the Volmer Heyrovsky mechanism, and in which the electrochemical desorption process is the rate-determining step [Eqs. (1)–(3)].<sup>[32]</sup>

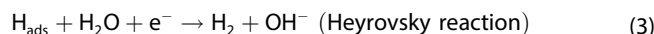
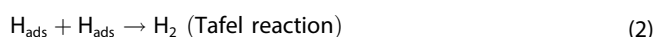
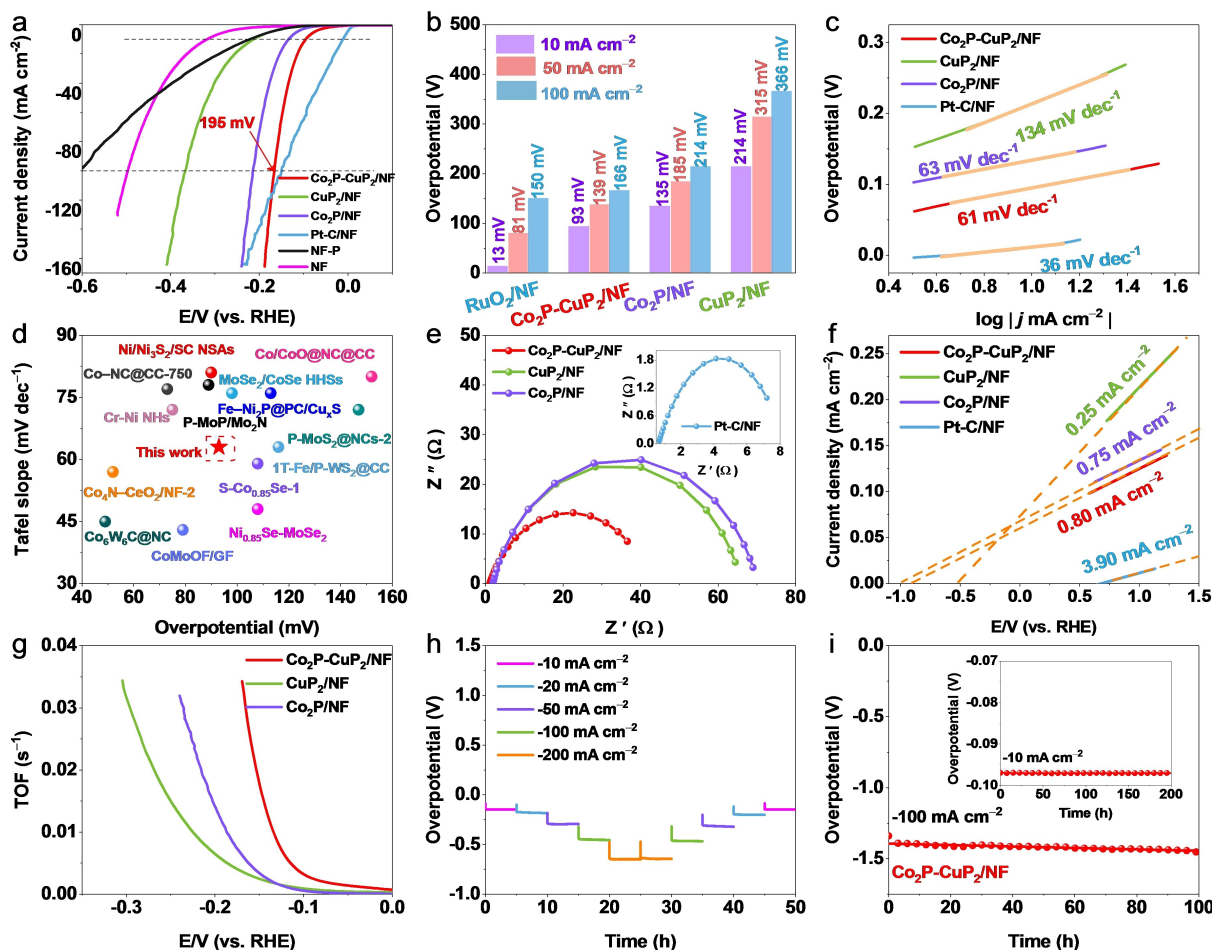


Figure 4d and Table S3 compare the overpotential observed in this work with the state-of-the-art reported overpotential of the HER catalyst at 10 mA cm<sup>-2</sup>. Obviously, the Co<sub>2</sub>P–CuP<sub>2</sub>/NF has achieved better HER performance. Meanwhile, a lower  $R_{ct}$  was observed for Co<sub>2</sub>P–CuP<sub>2</sub>/NF than all other control samples, demonstrating a lower resistance at the electrode-electrolyte interface, which results in rapid electron transfer kinetics (Figure 4e).<sup>[33]</sup> The exchange current density ( $j_0$ ) is calculated according to the Tafel slope to evaluate the intrinsic activity of the catalyst. The  $j_0$  of Co<sub>2</sub>P–CuP<sub>2</sub>/NF (0.80 mA cm<sup>-2</sup>) was significantly higher than Co<sub>2</sub>P/NF (0.75 mA cm<sup>-2</sup>) and CuP<sub>2</sub>/NF (0.25 mA cm<sup>-2</sup>), verifying that it has good intrinsic HER activity (Figure 4f).<sup>[32a]</sup> Furthermore, the turnover frequency (TOF) was calculated to assess the intrinsic HER activity (Figure 4g). Co<sub>2</sub>P–CuP<sub>2</sub>/NF manifested a higher TOF value, revealing the remarkable intrinsic activity.<sup>[34]</sup> The stability of Co<sub>2</sub>P–CuP<sub>2</sub>/NF was investigated by multistep chronopotentiometry. As depicted in Figure 4h, the voltage responds quickly and then



**Figure 4.** HER performance of prepared catalysts in 1.0 M KOH. (a) LSV polarization curves, (b) overpotentials comparison at 10, 50, and 100 mA cm<sup>-2</sup>, (c) corresponding Tafel slopes, (d) comparison with the overpotentials of state-of-the-art reported catalysts for HER activity at 10 mA cm<sup>-2</sup>, (e) electrochemical impedance spectroscopy (EIS), (f) exchange current density, (g) turnover frequency (TOF) value, and (h) multi-step chronopotentiometric curve at different current densities from 10 to 200 mA cm<sup>-2</sup> for Co<sub>2</sub>P–CuP<sub>2</sub>/NF, and (i) stability tests of Co<sub>2</sub>P–CuP<sub>2</sub>/NF electrodes.

remains stable when the current density changes suddenly. Similarly, the voltage presented a negligible attenuation after 50 h. Further, Co<sub>2</sub>P–CuP<sub>2</sub>/NF maintained stability for 100 and 200 h without significant attenuation at –100 mA cm<sup>-2</sup> and –10 mA cm<sup>-2</sup>, respectively, indicating outstanding durability (Figure 4i).

Encouraged by the excellent catalytic activity of both HER and OER, a two-electrode system assembly used Co<sub>2</sub>P–CuP<sub>2</sub>/NF as the cathode and anode for overall water splitting in 1.0 M KOH solution. The schematic diagram of Co<sub>2</sub>P–CuP<sub>2</sub>/NF for overall water splitting into two electrodes is presented in Figure 5a. As expected, the LSV polarization curve indicates that Co<sub>2</sub>P–CuP<sub>2</sub>/NF || Co<sub>2</sub>P–CuP<sub>2</sub>/NF delivers a voltage of 1.77 V and 2.38 V at 500 mA cm<sup>-2</sup> and 1000 mA cm<sup>-2</sup>, respectively, better than the RuO<sub>2</sub>/NF(+) || Pt/C/NF(–) (1.89 V@500 and 2.67 V@1000 mA cm<sup>-2</sup>) (Figure 5b). In addition, it was confirmed that the performance of Co<sub>2</sub>P–CuP<sub>2</sub>/NF at a current density of 10 mA cm<sup>-2</sup> outperformed most other electrocatalysts recently reported for overall water splitting, as shown in Figure 5c and Table S4. As shown in Figure 5d, the Co<sub>2</sub>P–CuP<sub>2</sub>/NF || Co<sub>2</sub>P–CuP<sub>2</sub>/NF reveals robust long-term durability at

100 mA cm<sup>-2</sup> for 160 h with almost no degradation. Moreover, the stability test was also conducted in a two-electrode system at high current densities of 600 mA cm<sup>-2</sup> and showed a good level of stability within 100 h (Figure S13). Furthermore, the XRD pattern of Co<sub>2</sub>P–CuP<sub>2</sub>/NF shows a similar pattern before and after OER and HER stability tests. (Figure S14). And the SEM also confirmed that it retained the previous nanosheet array structure with a small amount of aggregation (Figure S15), further proving that it has super durability. At the same time, XPS test showed that the surface chemical state of Co<sub>2</sub>P–CuP<sub>2</sub>/NF was almost the same before and after the stability test (Figure S16).

In the light of the above study, an alkaline Zn–H<sub>2</sub>O cell based on Co<sub>2</sub>P–CuP<sub>2</sub>/NF electrodes was fabricated.<sup>[35]</sup> Figure 6a illustrates that a commercial zinc sheet is employed as anode and Co<sub>2</sub>P–CuP<sub>2</sub>/NF as cathode, and 0.6 M KOH and 0.2 M Zn(Ac)<sub>2</sub> solution served as the electrolyte to assemble the Zn–H<sub>2</sub>O cell. As the cell begins to discharge, the HER reaction will proceed at the cathode to produce H<sub>2</sub>, while the zinc plate is oxidized to produce electricity at the anode.<sup>[36]</sup> The Co<sub>2</sub>P–CuP<sub>2</sub>/NF-based Zn–H<sub>2</sub>O cell provided an OCV of 0.93 V

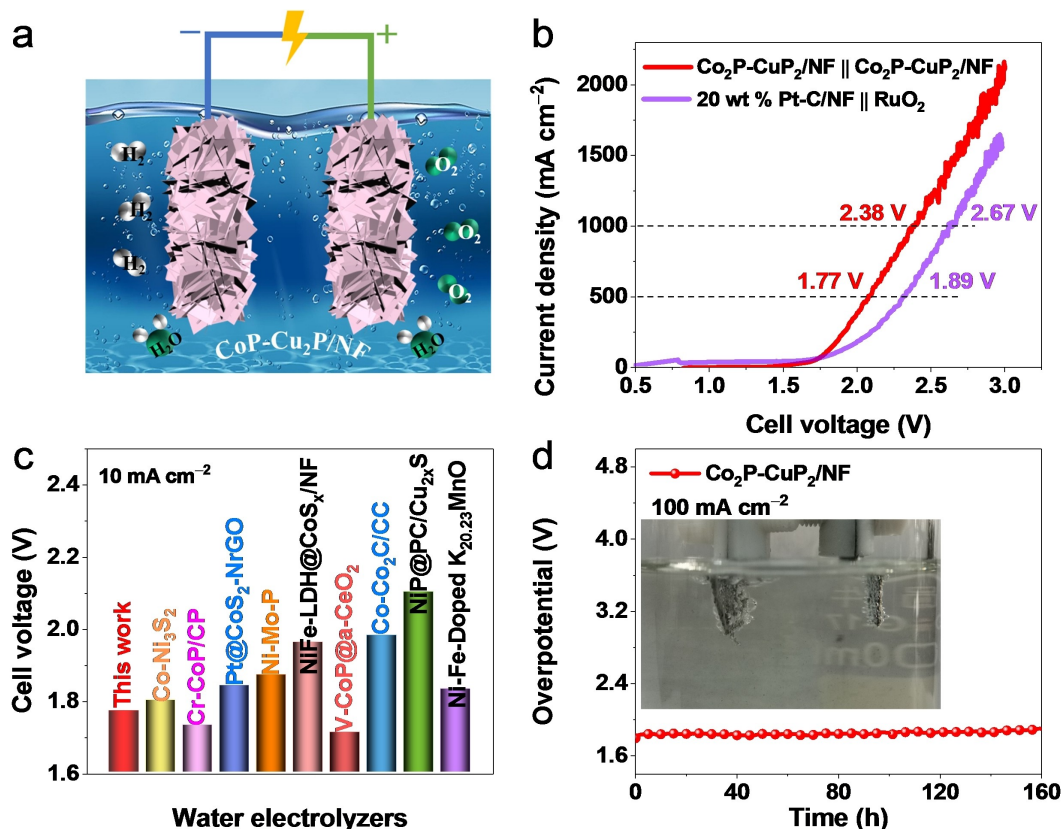


**Figure 5.** (a) Schematic diagram of overall water splitting electrolyzer using  $\text{Co}_2\text{P-CuP}_2/\text{NF}$  as bifunctional catalyst. (b) Comparison of polarization curves of  $\text{Co}_2\text{P-CuP}_2/\text{NF} \parallel \text{Co}_2\text{P-CuP}_2/\text{NF}$  and the  $\text{RuO}_2/\text{NF} \parallel \text{Pt-C/NF}$  at high currents in 1.0 M KOH. (c) Comparing cell voltages with the recently reported electrolyzers at  $10 \text{ mA cm}^{-2}$  in 1.0 M KOH. (d) Long-term stability test of  $\text{Co}_2\text{P-CuP}_2/\text{NF}$  at  $100 \text{ mA cm}^{-2}$  in 1.0 M KOH.

(Figures 6b and 6c) and reached a high power density of  $19.8 \text{ mW cm}^{-2}$  (Figure 6d), equivalent to commercial Pt-C/NF based Zn-H<sub>2</sub>O cell ( $26.9 \text{ mW cm}^{-2}$ ). Considerably, an LED screen (Figure 6e) and a red LED light (Figure 6f) can be lit by three or two Zn-H<sub>2</sub>O cells in series with  $\text{Co}_2\text{P-CuP}_2/\text{NF}$ , respectively, showing the potential application prospect of zinc-based energy.<sup>[37]</sup> Particularly, the  $\text{Co}_2\text{P-CuP}_2/\text{NF}$ -based Zn-H<sub>2</sub>O cell shows predominant long-term stability at  $10 \text{ mA cm}^{-2}$  for 120 h, indicating that the Zn-H<sub>2</sub>O cell possesses excellent durability (Figure 6g).

As discussed above, the superb OER/HER activity of  $\text{Co}_2\text{P-CuP}_2/\text{NF}$  in the alkaline electrolyte can be due to the following reasons: (i) Self-supporting binderless electrodes can minimize electrode resistance and promote electron diffusion. (ii) Staggered sheet-like heterostructure provide higher ECSA and more effective catalytically active sites. (iii) The strong electronic interaction between  $\text{Co}_2\text{P}$  and  $\text{CuP}_2$  can regulate the binding energy between the active sites and the intermediates, thereby enhancing the electrocatalytic activity.

## Conclusions

In summary, we report interfacial engineered  $\text{Co}_2\text{P-CuP}_2/\text{NF}$  catalyst for effective hydrogen and oxygen evolution. The

alkaline electrolyzer was constructed with  $\text{Co}_2\text{P-CuP}_2/\text{NF}$  heterostructure as the electrocatalyst that provides current densities of 500 and  $1000 \text{ mA cm}^{-2}$  at ultra-low cell voltages of 1.77 and 2.38 V, respectively. In addition, the alkaline Zn-H<sub>2</sub>O cell was fabricated with  $\text{Co}_2\text{P-CuP}_2/\text{NF}$  as the cathode, which can achieve a power density of  $26.9 \text{ mW cm}^{-2}$  and a long-term stability of 120 h. XPS results confirmed that the superior electrochemical performance was attributed to the redistribution of charge at the coupling interface caused by the electronic interaction between  $\text{Co}_2\text{P}$  and  $\text{CuP}_2$ . This work provides innovative ideas for constructing bimetal phosphide for effective dual-functional catalysts for efficient overall water splitting and Zn-H<sub>2</sub>O cell.

## Experimental

### Materials

Cobalt nitrate hexahydrate ( $\text{Co}(\text{NO}_3)_3 \cdot 6\text{H}_2\text{O}$ ), copper(II) chloride dihydrate ( $\text{CuCl}_2 \cdot \text{H}_2\text{O}$ ), ammonia ( $\text{NH}_3 \cdot \text{H}_2\text{O}$ ), ethanol absolute ( $\text{C}_2\text{H}_5\text{OH}$ ,  $\geq 99.7\%$ ), Nafion (5% solution), sodium hypophosphite monohydrate ( $\text{NaH}_2\text{PO}_2 \cdot \text{H}_2\text{O}$ , 99%), and potassium hydroxide (KOH) were purchased from Guangxi Zoey Biotechnology Co., Ltd. All reagents are analytical grade and were used without further purification. Commercial Pt/C (20 wt% for platinum) was purchased

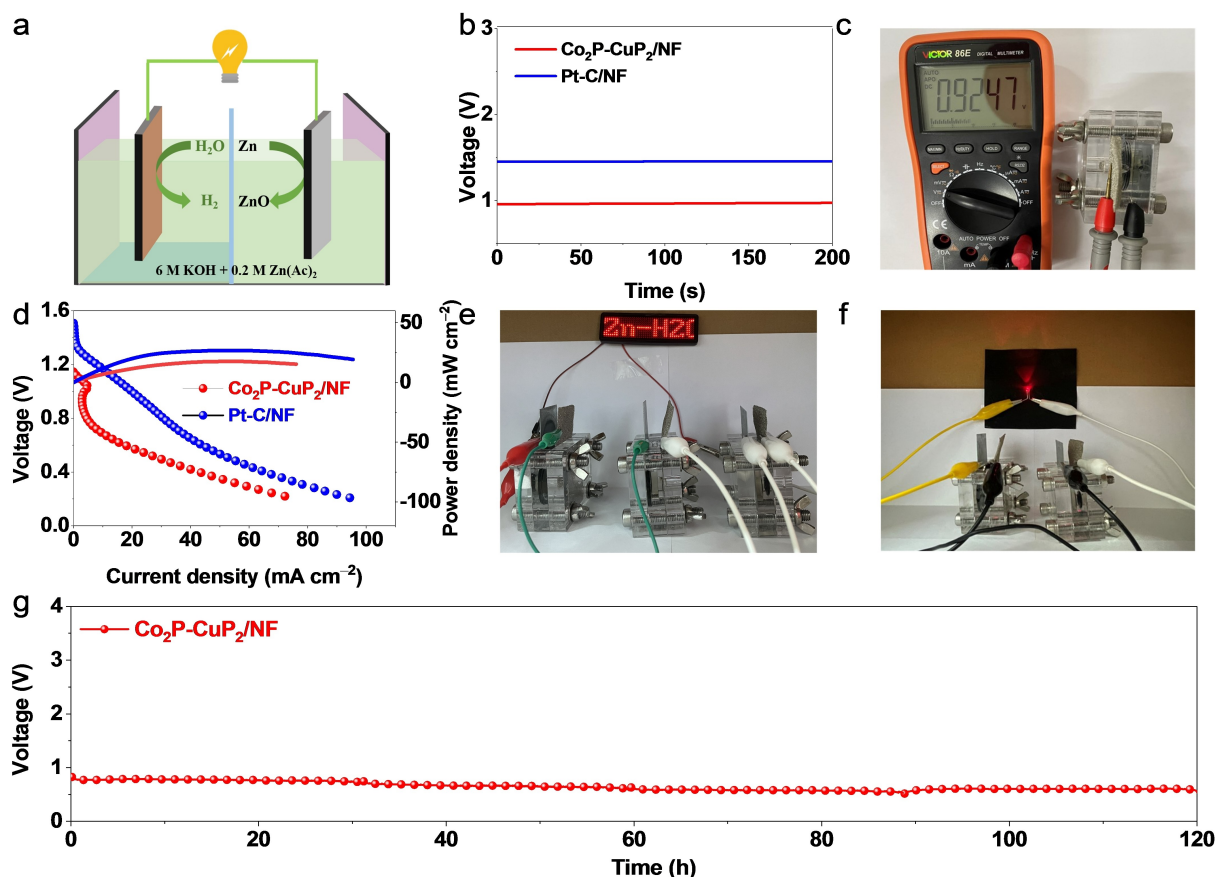


**Figure 6.** (a) Schematic diagram of Zn–H<sub>2</sub>O cell. (b) Open-circuit plots of Zn–H<sub>2</sub>O cell assembled with Co<sub>2</sub>P–CuP<sub>2</sub>/NF and Pt/C/NF, respectively. (c) Photo of the open circuit voltage (OCV) tested by the meter of Co<sub>2</sub>P–CuP<sub>2</sub>/NF. (d) Polarization curves and power densities of Co<sub>2</sub>P–CuP<sub>2</sub>/NF and Pt/C/NF. (e) Digital graph of LED screen lighted by three series of Co<sub>2</sub>P–CuP<sub>2</sub>/NF-based Zn–H<sub>2</sub>O cell. (f) Digital graph of a red light-emitting diode lighted by two series of Co<sub>2</sub>P–CuP<sub>2</sub>/NF-based Zn–H<sub>2</sub>O cell. (g) Long-term durability test at a current density of 10 mA cm<sup>-2</sup> of Zn–H<sub>2</sub>O cell using Co<sub>2</sub>P–CuP<sub>2</sub>/NF as cathode.

from Alfa Aesar. The Ni foam (NF) substrate used in the experiments has a thickness of 1.5 mm and a dimension of 3 cm × 1.5 cm.

### Synthesis of CuO on NF

The NF was ultrasonically washed with 0.5 M H<sub>2</sub>SO<sub>4</sub>, deionized water and ethanol for 15 min to remove impurities. CuO/NF was grown on NF by a chemical solution deposition technique. The solution was prepared by mixing 0.6 mmol of CuCl<sub>2</sub> in 15 mL deionized water in a 20 mL capacity glass vial and ultrasonically dissolving for 10 min to obtain a clear solution. Then 750 μL ammonia solution was added and sonicated for 10 min. Finally, an NF substrate was obliquely into in the vial then heated up to 80 °C for 2 h. After cooling to room temperature naturally, the obtained product was washed several times with deionized water and dried at room temperature for further use. In order to optimize the influence of the amount of Cu, different amounts of CuCl<sub>2</sub> (0.2, 0.4, 0.8, 1.0 mmol) were added under the same conditions.

### Synthesis of Co–Cu species on Ni foam

The samples were prepared *via* a facile one-step constant potential electrodeposition method in a standard three-electrode system with the prepared CuO (1 cm × 1.5 cm) as working electrode, platinum sheet and saturated calomel electrode as counter electrode and reference electrode, respectively. 0.1 mmol Co-

(NO<sub>3</sub>)<sub>3</sub>·6H<sub>2</sub>O was dissolved in 25 mL deionized water and ultrasonicated for 20 min to obtain the electrolyte. A typical constant potential electrodeposition was employed to synthesize Co–Cu sheet-like on the NF *via* a constant potential at –1.1 V versus the SCE for 5 min. After electrodeposition, the samples were washed with deionized water several times and dried naturally at room temperature.

### Synthesis of Co<sub>2</sub>P–CuP<sub>2</sub>/NF, Co<sub>2</sub>P/NF and CuP<sub>2</sub>/NF

Two pieces of Co–Cu species/NF (1 cm × 1.5 cm) and 1.0 g of NaH<sub>2</sub>PO<sub>2</sub>·H<sub>2</sub>O were placed downstream and upstream of the tube furnace, respectively. Subsequently, the tube furnace was heated slowly to 350 °C (5 °C min<sup>-1</sup>) under N<sub>2</sub> flow (20 sccm) for 2 h. Afterwards, the resultant products were rinsed with deionized water and dried at room temperature. The prepared sample was named as Co<sub>2</sub>P–CuP<sub>2</sub>/NF (from XRD data). The total loading of Co<sub>2</sub>P–CuP<sub>2</sub>/NF was about 9.82 mg cm<sup>-2</sup>. Different Co–Cu samples were prepared by controlling the electrodeposition time (3, 4, 6 and 7 min), which are herein labeled as Co<sub>2</sub>P–CuP<sub>2</sub>/NF-3 min, Co<sub>2</sub>P–CuP<sub>2</sub>/NF-4 min, Co<sub>2</sub>P–CuP<sub>2</sub>/NF-6 min, and Co<sub>2</sub>P–CuP<sub>2</sub>/NF-7 min, respectively.

For comparison, the synthesis process of Co<sub>2</sub>P/NF was similar to Co<sub>2</sub>P–CuP<sub>2</sub>/NF except that bare NF was applied as the electrodeposition substrate. CuP<sub>2</sub>/NF was obtained by direct phosphating

with CuO/NF as the precursor, using a similar method of  $\text{Co}_2\text{P}-\text{CuP}_2/\text{NF}$ .

### Synthesis of Pt–C/NF and $\text{RuO}_2/\text{NF}$

The homogeneous catalyst ink was obtained by mixing 2 mg  $\text{RuO}_2/\text{NF}$  or 2 mg Pt/C with 400  $\mu\text{L}$  of water/ethanol ( $V/V = 1:1$ ) and 10  $\mu\text{L}$  5% Nafion as a binder. Then, the mixture was drop-casted onto the NF surface (1 cm  $\times$  1.5 cm) and dried in the air.

### Characterization

X-ray diffraction (XRD, Rigaku D/Max-3c) was performed using a D/Max 2500 V PC with Cu  $K\alpha$  radiation (Rigaku, USA) to determine the composition of all samples. The scanning electron microscopy (SEM, Quanta FEG 200, Holland) and transmission electron microscopy (TEM, Talos F200S) were adopted to characterize the morphology of electrocatalysts. The energy-dispersive X-ray (EDX) spectroscopy was carried out to analyze the composition. The thickness of the sample was analyzed on the Bruker (Dimension ICON) scanning probe microscope by atomic force microscope (AFM). The actual metal contents in the various catalysts were examined by inductively coupled plasma mass spectroscopy (ICP-MS, PerkinElmer corporation, FLEXAR-NEXION300X). The element and surface valence states of the materials were analyzed by X-ray photoelectron spectroscopy (XPS, JPS-9010 TR Photo-electron Spectrometer, Japan).

### Electrochemical measurements

All electrochemical tests of the as-prepared catalysts were investigated using an electrochemical workstation of Bio-logic VMP3 and a conventional three-electrode cell configuration in 1.0 M KOH, in which catalyst was used as working electrode, graphite plate and saturated calomel electrode (SCE) were served as the auxiliary electrode and reference electrode, respectively. The prepared catalysts were electrochemically activated by cyclic voltammetry (CV) for 5 cycles at a scanning rate of 5  $\text{mVs}^{-1}$  to reach a stable state. Linear sweep voltammetry (LSV) measurement was carried out to obtain the polarization curves at a scan rate of 0.2  $\text{mVs}^{-1}$  for OER performance and 5  $\text{mVs}^{-1}$  for HER performance. Electrochemical impedance spectroscopy (EIS) was performed with scanning frequency ranging from 200 kHz to 10 mHz. Cyclic voltammetry (CV) at different scan rates was used to evaluate the electrochemically active surface area (ECSA) calculation of ( $C_{dl}$ ) values based on double-layer capacitance. The multi-step chrono-potentiometric curve was applied with the current density being increased from 10 to 200  $\text{mAcm}^{-2}$  (5 h per step). Chronoamperometry was used to assess the durability and long-term stability of the material. The following CV was performed at a scan rate of 5  $\text{mVs}^{-1}$ , and the average of the two potentials at the zero-crossing (1.040 V) of the current was considered to be the thermodynamic potential of 1.0 M KOH with  $\text{H}_2$ -saturated for about 10 min (Figure S1). Therefore, all the curves reported in this work have been calibrated by  $iR$  compensation, and all electrochemical tests were performed at room temperature ( $25 \pm 1^\circ\text{C}$ ).

### Acknowledgements

This work has been supported by the National Natural Science Foundation of China (no. 21965005), Natural Science Foundation of Guangxi Province (2018GXNSFAA294077,

2021GXNSFAA076001), Project of High-Level Talents of Guangxi (F-KA18015), and Guangxi Technology Base and Talent Subject (GUIKE AD18126001, GUIKE AD20297039).

### Declaration of Competing Interest

The authors declare that they have no known competing financial interests or personal relationships that could have appeared to influence the work reported in this paper.

### Data Availability Statement

Research data are not shared.

**Keywords:**  $\text{Co}_2\text{P}-\text{CuP}_2$  · Bimetallic phosphide · Sheet-like heterostructure · Overall water splitting ·  $\text{Zn}-\text{H}_2\text{O}$  cell

- [1] a) F. Yang, Y. Luo, Q. Yu, Z. Zhang, S. Zhang, Z. Liu, W. Ren, H.-M. Cheng, J. Li, B. Liu, *Adv. Funct. Mater.* **2021**, *31*, 2010367; b) Z.-W. Wei, H.-J. Wang, C. Zhang, K. Xu, X.-L. Lu, T.-B. Lu, *Angew. Chem. Int. Ed.* **2021**, *60*, 16622–16627.
- [2] B. Tian, H. Shin, S. Liu, M. Fei, Z. Mu, C. Liu, Y. Pan, Y. Sun, W. A. Goddard III, M. Ding, *Angew. Chem. Int. Ed.* **2021**, *60*, 16448–16456.
- [3] V. H. Hoa, D. T. Tran, S. Prabhakaran, D. H. Kim, N. Hameed, H. Wang, N. H. Kim, J. H. Lee, *Nano Energy* **2021**, *88*, 106277.
- [4] a) H. Song, M. Wu, Z. Tang, J. S. Tse, B. Yang, S. Lu, *Angew. Chem. Int. Ed.* **2021**, *60*, 7234–7244; b) Y. Liu, J. Zhang, Y. Li, Q. Qian, Z. Li, G. Zhang, *Adv. Funct. Mater.* **2021**, *31*, 2103673.
- [5] a) Y. Yang, Y. Xie, Z. Yu, S. Guo, M. Yuan, H. Yao, Z. Liang, Y. R. Lu, T.-S. Chan, C. Li, H. Dong, S. Ma, *Chem. Eng. J.* **2021**, *419*, 129512; b) B. Lu, J. Zang, W. Li, J. Li, Q. Zou, Y. Zhou, Y. Wang, *Chem. Eng. J.* **2021**, *422*, 130062.
- [6] S. Wen, G. Chen, W. Chen, M. Li, B. Ouyang, X. Wang, D. Chen, T. Gong, X. Zhang, J. Huang, K. Ostrikov, *J. Mater. Chem. A* **2021**, *9*, 9918–9926.
- [7] a) L. Yang, R. Liu, L. Jiao, *Adv. Funct. Mater.* **2020**, *30*, 1909618; b) F.-F. Li, J.-F. Gao, Z.-H. He, L.-B. Kong, *ACS Appl. Mater. Interfaces* **2021**, *13*, 10071–10088.
- [8] Y. Wang, B. Kong, D. Zhao, H. Wang, C. Selomulya, *Nano Today* **2017**, *15*, 26–55.
- [9] a) Q. Kang, M. Li, J. Shi, Q. Lu, F. Gao, *ACS Appl. Mater. Interfaces* **2020**, *12*, 19447–19456; b) K. Wu, Z. Chen, W. Cheong, S. Liu, W. Zhu, X. Cao, K. Sun, Y. Lin, L. Zheng, W. Yan, Y. Pan, D. Wang, Q. Peng, C. Chen, Y. Li, *ACS Appl. Mater. Interfaces* **2018**, *10*, 44201–44208.
- [10] J. Lin, Y. Yan, T. Xu, J. Cao, X. Zheng, J. Feng, J. Qi, *J. Colloid Interface Sci.* **2020**, *564*, 37–42.
- [11] L. Chai, Z. Hu, X. Wang, Y. Xu, L. Zhang, T.-T. Li, Y. Hu, J. Qian, S. Huang, *Adv. Sci.* **2020**, *7*, 1903195.
- [12] a) X. Jin, J. Li, Y. Cui, X. Liu, X. Zhang, J. Yao, B. Liu, *Inorg. Chem.* **2019**, *58*, 11630–11635; b) W. Li, Y. Jiang, Y. Li, Q. Gao, W. Shen, Y. Jiang, R. He, M. Li, *Chem. Eng. J.* **2021**, *425*, 130651.
- [13] Y. Hua, Q. Xu, Y. Hu, H. Jiang, C. Li, *J. Energy Chem.* **2019**, *37*, 1–6.
- [14] M. Jin, X. Zhang, R. Shi, Q. Lian, S. Niu, O. Peng, Q. Wang, C. Cheng, *Appl. Catal. B* **2021**, *296*, 120350.
- [15] D. Li, C. Zhou, R. Yang, Y. Xing, S. Xu, D. Jiang, D. Tian, W. Shi, *ACS Sustainable Chem. Eng.* **2021**, *9*, 7737–7748.
- [16] S. Riyajuddin, K. Azmi, M. Pahuja, S. Kumar, T. Maruyama, C. Bera, K. Ghosh, *ACS Nano* **2021**, *15*, 5586–5599.
- [17] A. G. Ramu, M. L. A. Kumari, M. S. Elshikh, H. H. Alkhamis, A. F. Alrefaei, D. Choi, *Chemosphere* **2021**, *271*, 129475.
- [18] B. T. Jebaslinhepybai, T. Partheeban, D. S. Gavali, R. Thapa, M. Sasidharan, *Int. J. Hydrogen Energy* **2021**, *46*, 21924–21938.
- [19] a) S. Chen, F. Wu, L. Shen, Y. Huang, S. K. Sinha, V. Srot, P. A. van Aken, J. Maier, Y. Yu, *ACS Nano* **2018**, *12*, 7018–7027; b) Y. Zhang, G. Wang, L. Wang, L. Tang, M. Zhu, C. Wu, S.-X. Dou, M. Wu, *Nano Lett.* **2019**, *19*,

- 2575–2582; c) G.-A. Li, C.-Y. Wang, W.-C. Chang, H.-Y. Tuan, *ACS Nano* **2016**, *10*, 8632–8644.
- [20] Y.-J. Tang, L. You, K. Zhou, *ACS Appl. Mater. Interfaces* **2020**, *12*, 25884–25894.
- [21] J. Kang, J. Sheng, J. Xie, H. Ye, J. Chen, X.-Z. Fu, G. Du, R. Sun, C.-P. Wong, *J. Mater. Chem. A* **2018**, *6*, 10064–10073.
- [22] a) M. C. Biesinger, *Surf. Interface Anal.* **2017**, *49*, 1325–1334; b) Q. Liu, Q. Liu, X. Kong, *ACS Appl. Mater. Interfaces* **2019**, *2*, 6000–6009.
- [23] a) Y. Zeng, J. Xue, M. He, C. Li, W. Zhu, S. Li, *Electrochim. Acta* **2021**, *367*, 137426; b) D. T. Tran, V. H. Hoa, H. T. Le, N. H. Kim, J. H. Lee, *J. Mater. Chem. A* **2020**, *8*, 14746–14756.
- [24] M.-T. Chen, J.-J. Duan, J.-J. Feng, L.-P. Mei, Y. Jiao, L. Zhang, A.-J. Wang, *J. Colloid Interface Sci.* **2022**, *605*, 888–896.
- [25] a) X. Du, J. Li, K. Tong, X. Zhang, *Dalton Trans.* **2021**, *50*, 6650–6658; b) J. Xiao, R. Qiao, Y. Zhang, X. Luo, *Int. J. Hydrogen Energy* **2021**, *46*, 31–40.
- [26] C. Wang, L. Qi, *Angew. Chem. Int. Ed.* **2020**, *59*, 17219–17224; *Angew. Chem.* **2020**, *132*, 17372–17377.
- [27] a) T. Kavinkumar, S. Seenivasan, H. Jung, J. W. Han, D.-H. Kim, *J. Mater. Chem. A* **2021**, *9*, 21132–21141; b) Y. Lin, K. Sun, S. Liu, X. Chen, Y. Cheng, W.-C. Cheong, Z. Chen, L. Zheng, J. Zhang, X. Li, Y. Pan, C. Chen, *Adv. Energy Mater.* **2019**, *9*, 1901213.
- [28] W. Zhang, Q. Jia, H. Liang, L. Cui, D. Wei, J. Liu, *Chem. Eng. J.* **2020**, *396*, 125315.
- [29] Y. Wang, G. Qian, Q. Xu, H. Zhang, F. Shen, L. Luo, S. Yin, *Appl. Catal. B* **2021**, *286*, 119881.
- [30] J. Zhou, L. Yu, Q. Zhou, C. Huang, Y. Zhang, B. Yu, Y. Yu, *Appl. Catal. B* **2021**, *288*, 120002.
- [31] Y. Lu, Z. Li, Y. Xu, L. Tang, S. Xu, D. Li, J. Zhu, D. Jiang, *Chem. Eng. J.* **2021**, *411*, 128433.
- [32] a) L. Yang, L. Huang, Y. Yao, L. Jiao, *Appl. Catal. B* **2021**, *282*, 119584; b) J. Zhang, X. Shang, H. Ren, J. Chi, H. Fu, B. Dong, C. Liu, Y. Chai, *Adv. Mater.* **2020**, *31*, 1905107.
- [33] J. Zhao, X. Ren, X. Sun, Y. Zhang, Q. Wei, X. Liu, D. Wu, *Chin. J. Catal.* **2021**, *42*, 1096–1101.
- [34] a) Y. Jiang, P. Sun, L. Sharma, B. Mao, R. Kakkar, T. Meng, L. Zheng, M. Cao, *Nano Energy* **2021**, *81*, 105645; b) C.-B. Hong, X. Li, W.-B. Wei, X.-T. Wu, Q.-L. Zhu, *Appl. Catal. B* **2021**, *294*, 120230.
- [35] P. Cai, Y. Li, G. Wang, Z. Wen, *Angew. Chem. Int. Ed.* **2018**, *57*, 3910–3915; *Angew. Chem.* **2018**, *130*, 3974–3979.
- [36] F. Cheng, L. Wang, H. Wang, C. Lei, B. Yang, Z. Li, Q. Zhang, L. Lei, S. Wang, Y. Hou, *Nano Energy* **2020**, *71*, 104621.
- [37] L. Wang, Z. Li, K. Wang, Q. Dai, C. Lei, B. Yang, Q. Zhang, L. Lei, M. K. H. Leung, Y. Hou, *Nano Energy* **2020**, *74*, 104850.

---

Manuscript received: December 20, 2021

Revised manuscript received: January 13, 2022

Accepted manuscript online: February 1, 2022

Version of record online: February 18, 2022